# Chapter 7
# Clouds and Aerosols in Saturn's Atmosphere

R.A. West, K.H. Baines, E. Karkoschka, and A. Sánchez-Lavega

**Abstract** In this chapter we review the photochemical and thermochemical equilibrium theories for the formation of condensate clouds and photochemical haze in Saturn's upper troposphere and stratosphere and show the relevant observations from ground-based and spacecraft instruments. Based on thermochemical equilibrium models we expect ammonia ice crystals to dominate in the high troposphere. There is very little spectral evidence to confirm this idea. Thanks to a stellar occultation observed by the Cassini VIMS instrument we now have spectral evidence for a hydrocarbon stratospheric haze component, and we still seek evidence for an expected diphosphine stratospheric haze component. The vertical distributions of stratospheric and upper tropospheric hazes have been mapped well with ground-based and Hubble Space telescope data, and Cassini data are beginning to add to this picture. Polar stratospheric aerosols are dark at UV wavelengths and exhibit strong Rayleigh-like polarization which suggests that auroral processes are important for their formation as is the case for the jovian polar stratospheric haze. The cloud and haze structure exhibits a variety of temporal variation, including seasonal change, long-term secular change near the equator, and short-term changes with a complicated latitudinal structure, and still not understood. Cassini instruments, especially the VIMS instrument, show an abundance of small-scale structure (convective clouds) at a pressure near 2 bar.

R.A. West and K.H. Baines
Jet Propulsion Laboratory, California Institute of Technology, CA, USA

E. Karkoschka
Lunar and Planetary Laboratory, University of Arizona, AZ, USA

A. Sánchez-Lavega
Departamento de Física Aplicada I, E.T.S. Ingenieros, Universidad del País Vasco, Spain

## 7.1 Introduction

Clouds and aerosols in planetary atmospheres are valuable for what they can tell us about important atmospheric chemical and physical processes. Clouds and aerosols play a role in the radiative and latent-heat terms of the energy budget, but to understand their radiative role one must have information on particle optical properties and the spatial distribution of opacity. Clouds can be used as tracers of motion to assess winds (see Chapter 6) and for that we would like to know pressure coordinates. In this chapter we start with a description of the expected vertical distributions and compositions of tropospheric clouds from thermochemical equilibrium theory and stratospheric haze from photochemistry. We examine observations made over the last three decades from the ground and from spacecraft which constrain particle optical and physical properties and vertical and horizontal distributions, and time variations of these quantities.

Images reveal three major latitude regimes and two major vertical regimes for clouds and aerosols. The troposphere and stratosphere constitute the two major vertical regimes, with the interface at the tropopause near 100 mbar. Different processes (cloud condensation/sublimation in a convecting atmosphere, and photochemical haze formation in a stably stratified atmosphere) dominate in the two locations. In terms of latitudinal distribution, the equatorial zone (generally between about $\pm 18°$) is a region of consistently high clouds and thick haze with little seasonal variation but with occasional major cloud outbursts. The polar regions north of about 60° contain a stratospheric haze that is optically thicker and darker than stratospheric haze at other latitudes, indicative of chemistry driven by auroral processes. Mid-latitude tropospheric clouds display substantial seasonal and nonseasonal variations. At middle and high latitudes small deep clouds which probably form in free convection are abundant in images of greatest atmospheric transparency. High spatial resolution limb images reveal distinct hazes layers at some latitudes. We will discuss all of these topics in more detail in the remainder of the chapter.

M. Dougherty et al. (eds.), *Saturn from Cassini-Huygens*,
DOI 10.1007/978-1-4020-9217-6_7, 

## 7.2 Expectations from Thermochemical Equilibrium Theory and Photochemistry

Oxygen, nitrogen and sulfur are the most abundant elements in solar composition which have the potential to combine with hydrogen to form clouds in the high troposphere. Lewis (1969) and Weidenschilling and Lewis (1973) were the first to offer quantitative models of the locations of condensate clouds based on thermochemical equilibrium theory. The guiding principal of these models is that solid or liquid phase condensation occurs at altitudes above the altitude where the temperature and partial pressure thermodynamically favors condensation. The models are complicated by solution chemistry in the ammonia–water cloud region and by uncertainties in the mixing ratios. Ammonia and hydrogen sulfide combine to form solid ammonium hydrosulfide ($NH_4SH$). Depending on the relative mixing ratios of $NH_3$ and $H_2S$, either the $NH_3$ or $H_2S$ could be entirely depleted above the haze layer by this process. It is believed that $H_2S$ is depleted and the remaining $NH_3$ is available to form an ammonia ice cloud at higher altitude. On Saturn the temperatures are cold enough to severely deplete ammonia gas at the level where visible and near-infrared photons sense and so gas absorption by ammonia is very weak.

The most recent thermochemical models were published by S. K. Atreya and colleagues. Figure 7.1 by Atreya and Wong (2005) shows cloud configurations for enhanced concentrations (by a factor of five over solar composition) for O, N and S. Clouds extend over a large vertical range. The base of the water–ammonia solution cloud is near 20 bar; that of the ammonium hydrosulfide cloud near 6 bar and the ammonia ice cloud base is near 2 bar. When the larger scale height, lower gravity and smaller $H_2$/He ratio relative to Jupiter are taken into account the clouds extend over a much larger vertical range relative to jovian clouds, and there is considerably more gas above the cloud bases than is the case for Jupiter. As a rule remote sensing does not probe as deeply as for Jupiter, but as discussed later images in window regions longer than about 0.7 μm detect clouds as deep as about 2 bars at locations where the diffuse haze particle number density is low.

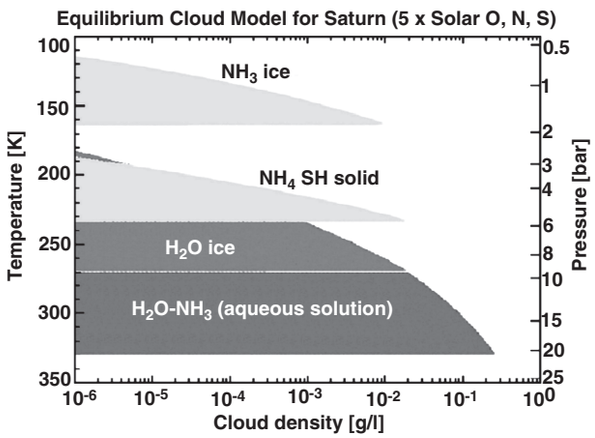


**Fig. 7.1** This graphic schematically illustrates the vertical locations and compositions of condensate clouds in Saturn's atmosphere based on thermochemical equilibrium models assuming O, N, and S enrichments by a factor of five over solar composition. Cloud density expressed on the ordinate is the result of a model which neglects sedimentation or vertical mixing or advection (from Atreya and Wong (2005))

Thermochemical model results such as those shown in Fig. 7.1 provide guidance to the possible locations of condensate clouds. However, local meteorology has a large influence on the locations of clouds. Experience with water clouds in the terrestrial atmosphere shows that cloud formation can be inhibited or that multiple layers can form depending on local temperature and water content. Experience with the Galileo probe (and ground-based observation dating to 1975 – see West et al. 1986) shows that regions of descending air suppress cloud formation, although layers can still form at altitudes above those predicted for a quiescent atmosphere with enhanced abundance of volatiles. Nor do these models take into account cloud microphysical processes. Because the detailed information needed for such models is lacking the best we can do is outline the range of possibilities. West et al. (2004) reviewed cloud microphysics models for Jupiter.

Stratospheric aerosols owe their origins primarily to photochemical processes and bombardment by energetic particles, especially in the auroral zones. Cosmic dust particles impact the upper atmosphere, although their contribution is probably small relative to the other sources. We do not have a detailed model to account for all of the processes, and the roles of energetic particles and ion chemistry are not well understood. Yet a collection of ideas has emerged regarding stratospheric aerosol formation. In Chapter 5, Fouchet et al. give a comprehensive review of photochemical processes. Here we mention the main ideas via Fig. 7.2 from Atreya and Wong (2005). Figure 7.2 was generated for Jupiter but the chemical paths (with the exchange of $PH_3$ and $P_2H_4$ for $NH_3$ and $N_2H_4$) carry over to Saturn. On Saturn the ammonia mixing ratio is too low to consider the production of $N_2H_4$ and instead phosphine photochemistry leading to diphosphine is important. Two types of hydrocarbons might be produced – a linear chain shown as the polymerization of acetylene ($C_2H_2$) and ring molecules starting with benzine ($C_6H_6$) and leading to more complex polycyclic aromatic hydrocarbons (PAHs). Friedson et al. (2002) produced a detailed model of hydrocarbon haze formation for Jupiter. The concept should apply to Saturn.

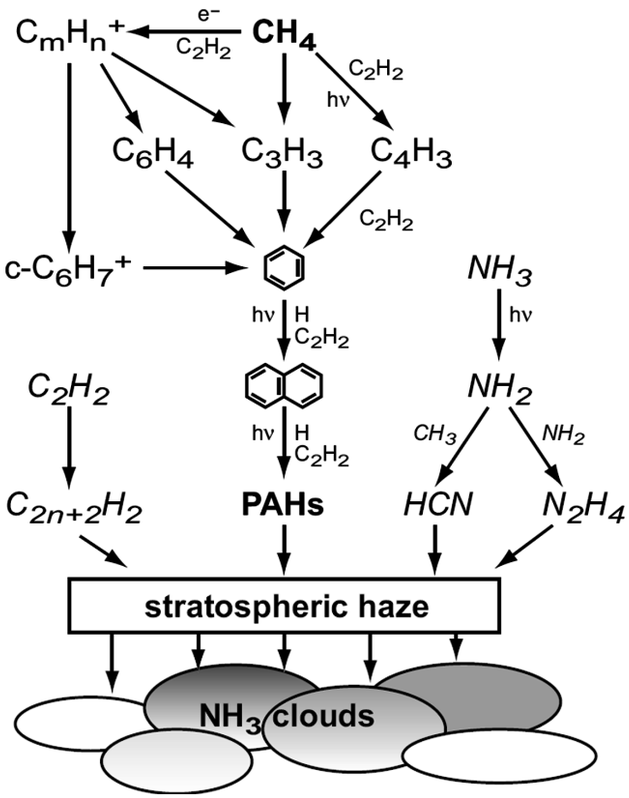


**Fig. 7.2** A simplified rendering of the chemical schemes leading to the formation of stratospheric aerosols, this graphic was created for the Jupiter atmosphere. It can also be applied to Saturn if $NH_3$ and $N_2H_4$ map to $PH_3$ and $P_2H_4$. Note the two paths for hydrocarbons leading to linear chains (polyacetylenes) or polycyclic aromatic hydrocarbons (PAHs). Energetic photons and particles acting on methane or phosphine may initiate the process (from Atreya and Wong (2005); see also Wong et al. (2003))

## 7.3 Observational Constraints on Particle Composition and Chromophores

From thermochemical equilibrium models we expect that ammonia ice particles dominate clouds near the top of the troposphere. Spectral signatures for ammonia ice are therefore expected. Laboratory measurements (Martonchik et al. 1984) show ammonia ice spectral features at several wavelengths in the near-infrared and at 9.4 and 26 μm in the thermal infrared. Although methane and hydrogen gas absorptions interfere with detection it is remarkable that no features have been observed. Some were observed for Jupiter as reported by Brooke et al. (1998), Baines et al. (2002) and Wong et al. (2004). Spatially-resolved observations show these features to be limited to a small fraction of the cloud coverage, typically in what are thought to be newly-forming cloud regions. For both Jupiter and Saturn and especially for Saturn it is a major puzzle that we do not see more widespread spectral signatures of ammonia ice.

Several factors might conspire to mask ammonia ice spectral signatures. If the particles are large (of order 10 μm radius or larger) so much light is absorbed in the wings of the band that it is hard to detect because the feature is very broad and overlaps atmospheric absorption features. Brooke et al. (1998) believe this is the case for jovian cloud particles. If a layer of smaller particles overlays the larger particles, and if the optical depth of this layer is sufficiently large we can expect to see an ammonia ice signature. Spectroscopic evidence discussed later indicates that particles near the top of the troposphere have mean radius closer to 1 μm.

Particle non-spherical shape is another factor which might diminish an ammonia ice spectral signature, at least for those features that are sensitive to particle shape. Huffman and Bohren (1980) called attention to the shape effect for spectral features formed when surface modes dominate electro-magnetic resonances. This effect is important even for particles smaller than the wavelength (in the Rayleigh approximation). Spectral features can be broadened further by a distribution of particle shapes. West et al. (1989) explored this idea for ammonia features at 9.4 and 26 μm. The peak of the absorption dropped by a factor of 2 while the width increased for the 26 μm-feature. Whether or not the shape effect is able to thwart detection remains to be seen, but it seems unlikely that this will suffice. The peak at 9.4 μm is shifted for tetrahedral particles relative to spheres but its magnitude is not diminished. It therefore seems that shape effects alone do not account for the non-detection.

Spectral features can be masked by a foreign contaminant, either from below (water or ammonium hydrosulfide brought up from depth) or from above (photochemical products from the stratosphere). West et al. (1989) considered this possibility and found that the bulk composition of the particle must be dominated by the foreign contaminant if the resonant feature of the ammonia ice is to be significantly suppressed. Recently Atreya et al. (2005) and Kalogerakis et al. (2008) examined photochemical production rates relevant to the jovian atmosphere. Although they were able to estimate photochemical production rates they did not estimate formation rates for ammonia ice. In order for the photochemical component to be comparable to or dominate the ammonia ice component the formation rates for photochemical components must be greater than that for ammonia ice. On Saturn hydrocarbon photochemistry is operative as it is for Jupiter (although with a solar flux down by a factor of almost four but with a different methane mixing ratio in the high atmosphere, depending on the details of diffusive separation above the homopause and the depth of penetration of photolyzing radiation. Hydrocarbon haze may not be the most important contributor. Diphosphine ($P_2H_4$) is perhaps more important (Fouchet et al., this volume). No spectral signatures of solid $P_2H_4$ have been reported. If a coating or condensation nucleus is responsible for the suppression of ammonia ice spectral features it means

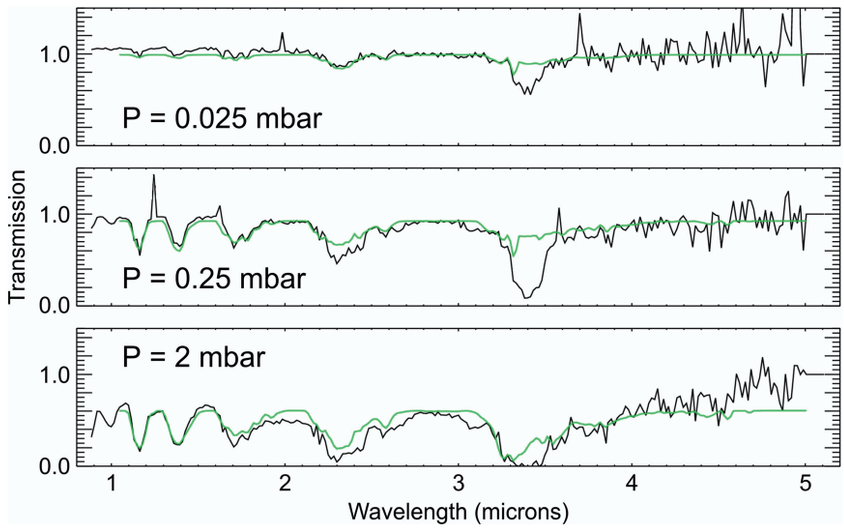


**Fig. 7.3** The black curves are observed signal ratios (occulted signal divided by unocculted signal) at three tangent-point pressures in the atmosphere. The green curves are model calculations (from Nicholson et al. (2006))

that we are seeing a photochemical haze, not an ammonia cloud, in images of Saturn.

Spectroscopic evidence for a hydrocarbon haze in Saturn's stratosphere was observed in a stellar occultation experiment performed by the Cassini VIMS instrument (Nicholson et al. 2006). The signal from the starlight passing through the atmosphere was divided by the signal taken a few moments earlier without any attenuation by the atmosphere. Instrument sensitivity drops out of the ratio making the experiment insensitive to calibration issues. Figure 7.3 shows the ratio for three values of the pressure level of the ray tangent point. Models of the methane absorption account for nearly all of the absorption features. A feature at 3.4 μm reveals a hydrocarbon haze, probably a linear chain (polyacetylene) rather than a ring (benzene or a polycyclic aromatic; P. Nicholson, private communication 2008). The occultation sampled a middle latitude. It is possible that benzene and PAHs are more abundant in the auroral zone/polar vortex regions where energy input from the auroras is substantial.

If one accepts the notion that a coating of stratospheric haze material is responsible for the suppression of ammonia ice spectral features it is tempting to think that such haze material might also be responsible for the dusky yellow/light-brown/red hue of most of Saturn at visible wavelengths. Identification of the chromophore material is ambiguous because there are no narrow spectral signatures, only a broad darkening from the red to blue wavelengths. Hydrocarbon chromophores which absorb at visible wavelengths might be derived from polyacetylene or PAH molecules that have undergone some modification due to solid-state photochemistry, driving off H and increasing the C/H ratio. Materials with higher C/H ratios absorb light more efficiently. Black carbon is an end member. A table of candidate materials (including inorganics) and references to the original proposals and laboratory measurements can be found in table V of West et al. (1986).

Compounds involving sulfur, hydrogen, and nitrogen have also been proposed as coloring agents for Jupiter and Saturn. These materials would be brought up from several bars pressure where they exist in the gas phase, or as $NH_4SH$ solid. Solid-state photochemistry would be required to modify the composition because $NH_4SH$ solid is white. Perhaps the best observational support for this hypothesis comes from images which show localized dark spots associated with vortices (see Fig. 7.4). Upwelling of deeper S- and N-rich gas or $NH_4SH$ cloud particles with exposure to UV light at the top of the cloud seems the simplest mechanism to account for such localized dark albedo associated with vortices. These features are relatively bright in strong methane absorption bands which indicates that the clouds are higher and thicker than their surroundings as expected for upwelling.

Images like those in Fig. 7.4 underscore the fact that we do not have a good understanding of the relationship between atmospheric dynamics, particle microphysics, and chromophore genesis, distribution or exposure. For Jupiter West et al. (1986) proposed that chromophores are ubiquitous and that marginally stable ammonia condensation/sublimation cycles involving coating chromophore cloud condensation nuclei could account for rapid changes in color and albedo with unobservably small change in temperatures or wind. The idea advanced by Atreya et al. (2005) takes the opposite approach – it is the coating of ammonia by a photochemical material that dominates. That idea seems more attractive for Saturn if the formation rate of the photochemical product is larger than the formation rate of ammonia ice particles, but still lacking is an understanding of small-scale color and albedo contrasts associated with vortices and other features.

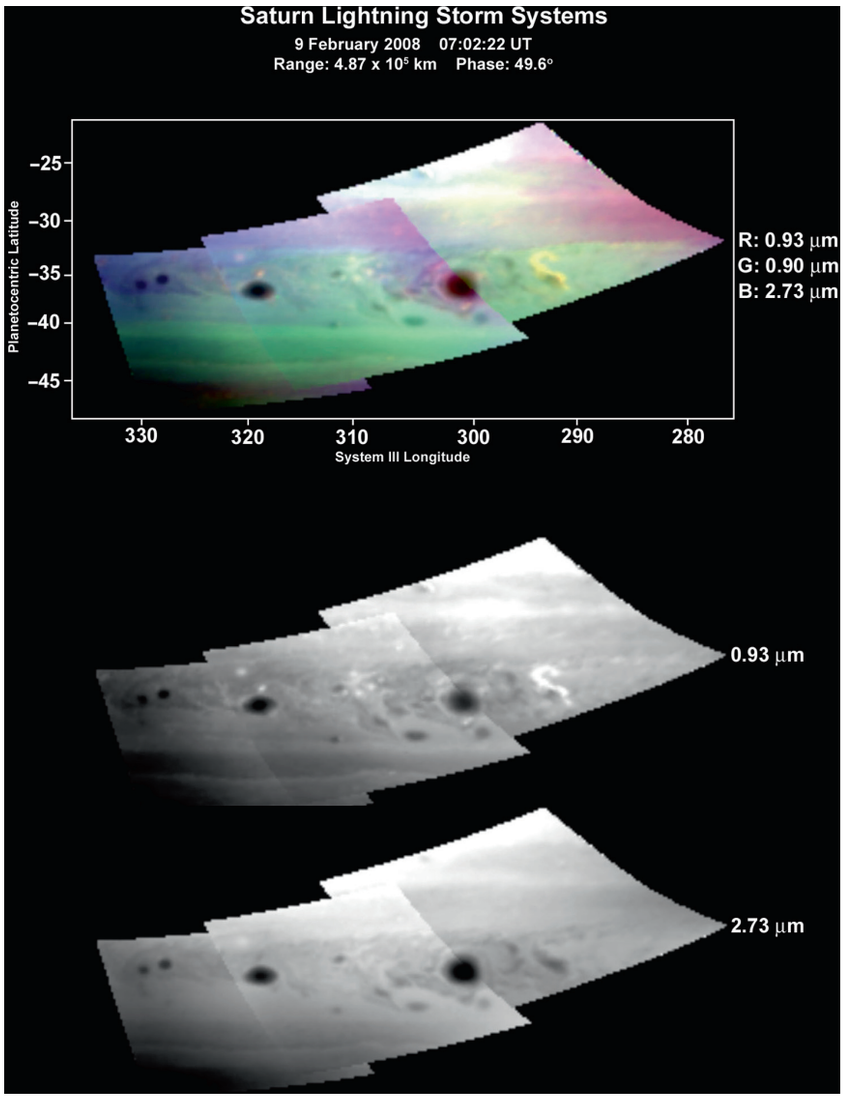


**Fig. 7.4** These images from the Cassini VIMS experiment show both dark and bright features at two window regions (between methane bands) in the near-infrared. At least some of the features (most notably the bright cloud in the shape of a mirror-reversed question mark) are associated with a lightning storm. Most spots are dark at both wavelengths. The mirror-reversed question mark is bright in the 0.93-μm window but not in the 2.73-μm window. Its relatively high reflectivity at 0.93 μm suggests that it is a region where an ammonia ice cloud formed recently and the ratio of ammonia cloud to chromophore material is higher than in the surrounding region (adapted from Baines et al. (2009))

## 7.4 Aerosol Optical and Physical Properties

Information on particle optical and physical properties comes from the wavelength dependence of the extinction and scattering cross sections, the scattering phase function and possibly the polarization. The accumulated spacecraft and ground-based data offer the potential to retrieve this information on fine spatial scales, but thus far particle phase functions and polarization curves have been retrieved for only two latitude bands using data from the Pioneer 11 spacecraft. Analyses of optical properties at low phase angles has been performed using data from the Hubble Space Telescope (HST) for many latitudes over a time span of several years and these provide clues to time variations over short and long time scales.

Knowledge of particle scattering phase functions is useful not only for particle size studies. Knowledge of the phase function is as important as the optical depth profile for estimates of solar energy deposition and in line formation used to infer chemical abundances from reflected sunlight. Figure 7.5 shows phase functions derived from data for the Equatorial Zone and for a mid-latitude belt from Pioneer 11 data (Tomasko and Doose 1984). The curves shown in Fig. 7.5 are double Henyey–Greenstein functions with forward and backward peaks. The best-fit Henyey–Greenstein parameters are listed in Table 7.1. Note that the fits are based on measurements at scattering angles greater than 30°. The diffraction peak for particles much larger than the wavelength is confined to smaller angles, so it is difficult to gauge particle size if the mean radius is more than a few times the wavelength. It

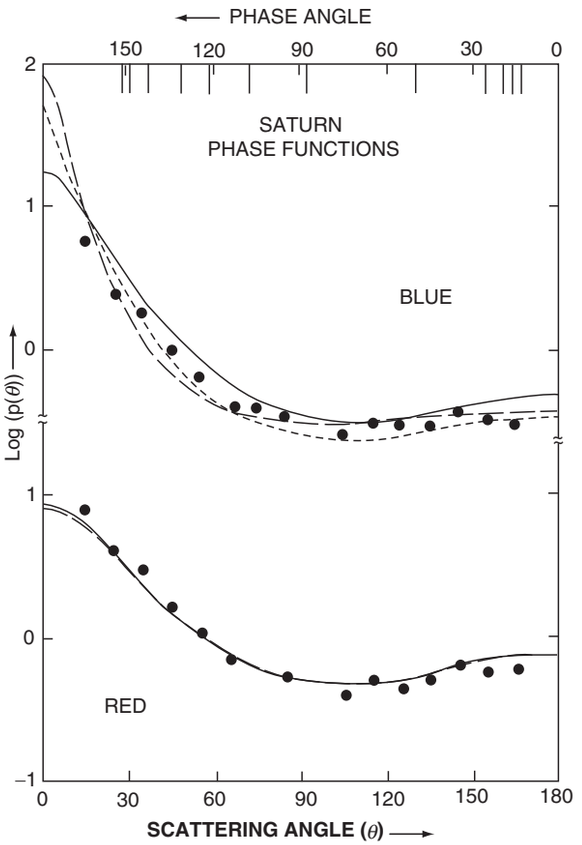


**Fig. 7.5** Particle scattering phase functions derived for Saturn aerosols for the Equatorial Zone (*solid curves*) and for a mid-latitude belt (*dashed curves* with cloud-top pressures at 150 and 250 mbar). The dots are from laboratory measurements of 10-μm ammonia ice particles grown in a laboratory chamber (Pope et al. 1992) (from Tomasko and Doose (1984))

**Table 7.1** Double Henyey–Greenstein (Henyey and Greenstein, 1941) phase function parameters for a Belt and Zone from Tomasko and Doose (1984). Eqs. 7.2 and 7.3 of the text give the functional form. Two sets of parameters were derived for the belt at 15–17° S for two possible values of the pressure at the top of the haze layer ($P_0$). The aerosol albedo for single scattering is given by ω. The parameter p is the geometric albedo for a homogeneous spherical body with the derived cloud properties and q is the phase integral. $F_0$ is a parameter for the absolute calibration of the photopolarimeter instrument

| Parameters of Best-fitting Phase Functions | | | | | | |
|---|---|---|---|---|---|---|
| | 7°S–11°S | | 15°S–17°S | | | |
| | Red | Blue | Red | | Blue | |
| $P_o$ | 150 mb | 150 mb | 150 mb | 250 mb | 150 mb | 250 mb |
| $g_1$ | 0.620 | 0.710 | 0.603 | 0.633 | 0.870 | 0.824 |
| $g_2$ | −0.294 | −0.317 | −0.302 | −0.286 | −0.116 | −0.231 |
| $f$ | 0.763 | 0.860 | 0.768 | 0.776 | 0.764 | 0.862 |
| $\varpi$ | 0.986 | 0.920 | 0.986 | 0.986 | 0.920 | 0.920 |
| $F_o$ | 85.6 | 50.8 | 80.1 | 80.9 | 51.2 | 50.3 |
| $p$ | 0.501 | 0.287 | 0.502 | 0.496 | 0.264 | 0.276 |
| $q$ | 1.41 | 1.43 | 1.41 | 1.41 | 1.45 | 1.41 |

is also important to recognize that the derived phase function at small scattering angles is limited to aerosols near the top of the haze layer. Rayleigh scattering from gas above the haze can introduce ambiguity in the retrieved phase function if the vertical location of the haze is uncertain and this accounts for the two models for the blue belt in Table 7.1. The use of the double Henyey–Greenstein phase function is justified because the particles are expected to be solid and therefore not spheres. Spherical particles have a deep minimum at middle scattering angles if the particle radius is larger than the wavelength and this behavior is not present for nonspherical particles which have a shallow minimum. Spherical particles larger than the wavelength also have rainbow and glory features which are either not present or weak for nonspheres. Phase functions for both spherical and nonspherical particles have a similar shape in the forward diffraction region which is controlled by the particle projected area.

Comparison with laboratory measurements for ammonia ice crystals (Pope et al. 1992) shown in Fig. 7.5 suggests that the particles which form the main haze layer have effective radii near 10 μm. While this result may be correct it seems likely that a broad range of particle size is allowed by the observations provided the mean radius is larger than visible wavelengths.

Particle polarization also supports the idea that the particles are not small compared to the wavelength. Polarization as measured by the Pioneer 11 Imaging Photopolarimeter (IPP) has a negative branch (see Fig. 7.6) at red wavelengths. Here again there is some ambiguity due to uncertainty in the vertical structure. Pope et al. (1992) infer from laboratory measurements that the particles in the main haze layer are large (size parameter $2\pi \cdot \text{radius}/\text{wavelength} \sim 10$–$50$).

The Cassini ISS obtained images using polarizers at wavelengths from the near-UV to the near-IR. Some of the earliest images (Fig. 7.7) show positive polarization at high southern latitudes, similar to what was seen for Jupiter. At middle and low latitudes the polarization is negative at the phase angle of the images (60.7°). Polarization is enhanced and the angle becomes positive near the limb and terminator indicating an optically thin layer of positively-polarizing particles and/or gas above the main negatively polarizing haze layer. This behavior was also noted by Tomasko and Doose (1984).

West and Smith (1991) noted that the jovian polar aerosols have strong positive polarization and strong forward scattering, like the haze in Titan's stratosphere. This combination of optical properties cannot be matched by spheres. West and Smith proposed that the particles are aggregates of small (∼tens of nm radius) monomers. The observation shown in Fig. 7.7 suggests that particles of this type are also abundant at high latitudes in Saturn's atmosphere, although it is not yet

known if they have strong forward scattering. The presence of these particles in polar regions for both Jupiter and Saturn suggests that auroral energy deposition is important in their formation. Pryor and Hord (1991) advocated this idea based on low UV reflectivity which is consistent with a hydrocarbon composition for these particles.

Observations from the Hubble Space Telescope have also shed some light on the nature of the polar stratospheric aerosol. The ultraviolet reflectivities are low at large angles of reflection, when observing near the limb of Saturn, these dark aerosols must extend up to pressures of a few millibar, because the Rayleigh scattering from a clear layer of some 10–20 mbar would make Saturn brighter than observed.

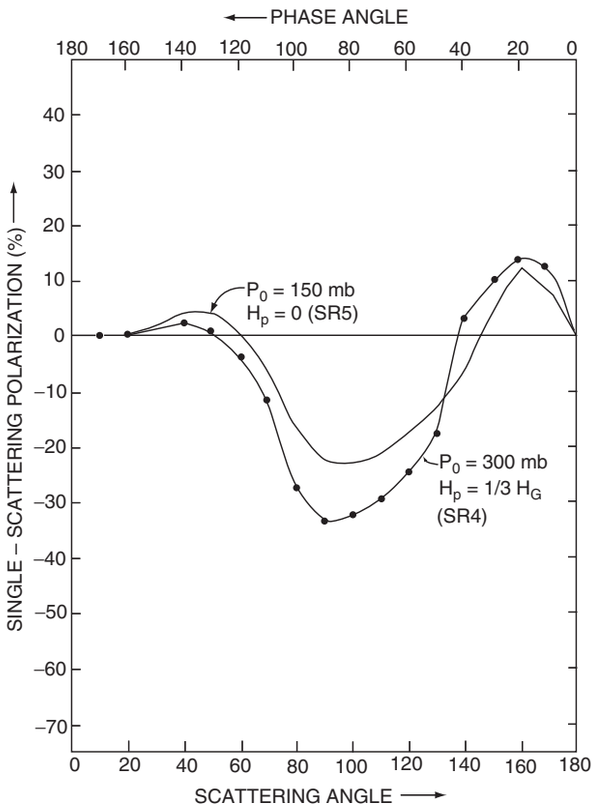


**Fig. 7.6** Polarizing function for the Equatorial Zone in red light for two values of the pressure at the top of the main haze layer ($P_0$) and for two values of the particle scale height $(H_p)$ (from Tomasko and Doose (1984))

These aerosols can be seen in deep methane bands such as the 890 nm methane band, but their inferred optical depths at these near-infrared wavelengths are many times lower than at ultraviolet wavelengths (Fig. 7.8). Assuming spherical particles, Karkoschka and Tomasko (1993) found a mean aerosol radius of 0.15 μm for the aerosols near the North Pole, and Karkoschka and Tomasko (2005) and Pérez-Hoyos et al. (2005) gave values of 0.15 and 0.1 μm for the aerosols near the South Pole, respectively assuming the particles are spheres.

The imaginary refractive index of the polar stratospheric aerosols is about 0.1 at 300 nm wavelength with a steep wavelength dependence, approximately following a power law with wavelength with an exponent of −6.5 (Karkoschka and Tomasko 2005). This yields a single scattering albedo near 0.9 at 300 nm wavelength, increasing to 0.99 at 450 nm.

Between −65° and 65° latitude, many observations require some aerosol component in the stratosphere. However, the optical depth is down by a factor of about 4 compared to aerosols at the polar latitudes. This makes it much harder to determine the aerosol properties. Assuming that both types of stratospheric aerosol have the same properties has yielded reasonable fits to observations (Karkoschka and Tomasko 2005). However, the constraints are not tight. These aerosols may originate by solar ultraviolet radiation. Since the formation processes of both kinds of stratospheric aerosols are different, the aerosol properties could be somewhat different too. The strongest observational constraint on the low-latitude aerosols indicate that their size must be quite small too, about 0.1–0.2 μm radius assuming spherical shape (Muñoz et al. 2004; Pérez-Hoyos et al. 2005).

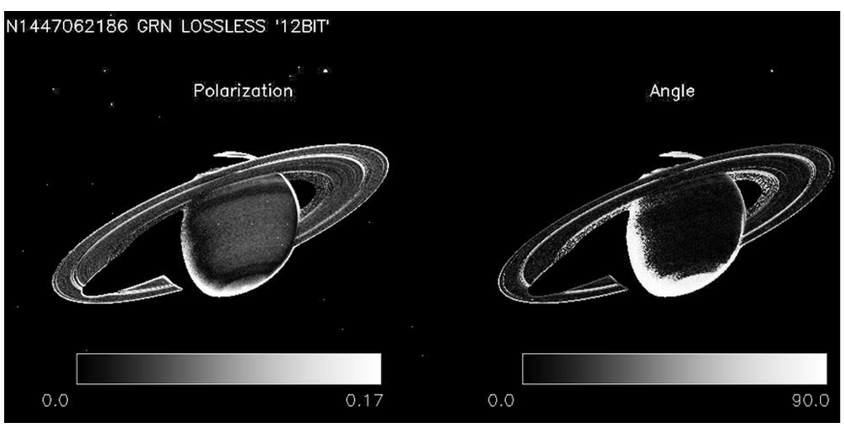


**Fig. 7.7** Polarization images in the Cassini ISS Narrow-angle camera Green filter obtained in 2003 show enhanced positive polarization (angle of the electric vector near 90° with respect to the scattering plane) at high southern latitudes

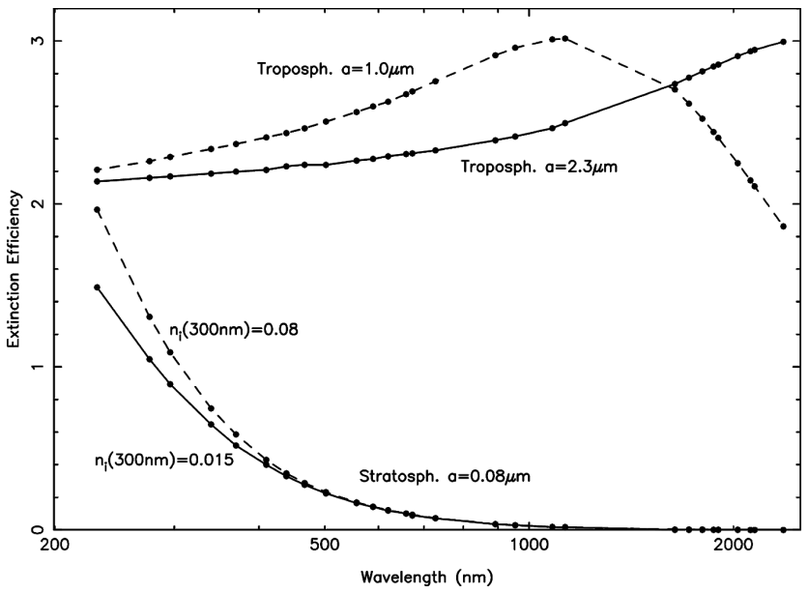


**Fig. 7.8** Extinction efficiency as function of wavelength for four sample aerosol parameters. The tropospheric aerosol sizes of 1.0 and 2.3 μm are typical for mid-latitudes in 1995 and 2003, respectively. The stratospheric imaginary refractive indices of 0.015 and 0.08 at 300 nm wavelength are typical for low latitudes and polar latitudes, respectively (from Karkoschka and Tomasko (2005))

## 7.5 Aerosol Vertical Structure

### *7.5.1 Radiative Transfer Models and Haze Structure*

Several techniques provide information on cloud and haze vertical structure. At visible and near-infrared wavelengths vertical sounding is possible via sampling in methane bands of various strengths. Although some have computed 'weighting functions' or 'contribution functions' these actually depend on the aerosol distribution and so are not well defined as they are for thermal temperature sensing although in the limit of single scattering one can use this technique as Stam et al. (2001) have done. In the general case which involves multiple scattering the vertical resolution of these techniques is typically of order one scale height. Other techniques such as stellar occultation (e.g. Fig. 7.3) or limb imaging provide much finer resolution in the vertical.

A sense of the depth of probing at different wavelengths can be obtained from Fig. 7.9 which shows optical depth 1/2 levels for Rayleigh scattering and methane absorption throughout the visible and near-infrared. At short wavelengths Rayleigh scattering is an important opacity source. The relation between Rayleigh optical depth and pressure was derived for Jupiter by West et al. (2004). A scaling argument leads to the following expression for Saturn.

$$\tau_R = P \cdot (24.4/g) \cdot \left(2.27 \cdot 10^{-3}/\mu\right) \cdot ([H_2]/0.86) \cdot 0.0083 \left(1 + 0.014\lambda^{-2} + 0.00027\lambda^{-4}\right) \cdot \lambda^{-4} \quad (7.1)$$

where $\lambda$ is the wavelength in μm, P is the pressure in bar, g (m $s^{-2}$; a function of latitude) is the local effective acceleration accounting for both gravitation and rotation (see Chapter 4), μ is the mean molecular weight $\left(\text{kg mole}^{-1}\right)$ and $[H_2]$ is the $H_2$ mole fraction. The dependence on mean molecular weight and $H_2$ mole fraction is made explicit so that the equation can be used as the helium mole fraction becomes better defined (see the Chapter 5). We neglected terms of order $[H_2]^2$ which is probably acceptable in view of the uncertainty in the He mole fraction.

The method employed by Stam et al. retrieves a product of the aerosol density times the optical cross section times the particle single-scatter albedo times the phase function at the scattering angle of the observation (near 180° for the Stam et al. paper). It is impossible to know the value of each term in the product and so the method provides a measure of aerosol variations with latitude and altitude if the optical properties do not change with wavelength, or if their wavelength dependence can be estimated. Banfield et al. (1998) pioneered this method for Jupiter. The method does not make assumptions about how many layers are present or at what levels but it requires that multiple scattering be small relative to single scattering, which means that it is limited to strong absorption bands. Aerosol number density or optical depth can be inferred if the particles are assumed to be spheres. Derived aerosol distributions are shown in Fig. 7.10 which shows hemispheric asymmetry in 1995 near equinox for both stratosphere and troposphere haze layers.

The strategy employed by most investigators to retrieve the optical properties and vertical structure of the aerosols is to fit the center-to-limb variation (CTLV) curves at selected wavelengths to those obtained from a radiative transfer

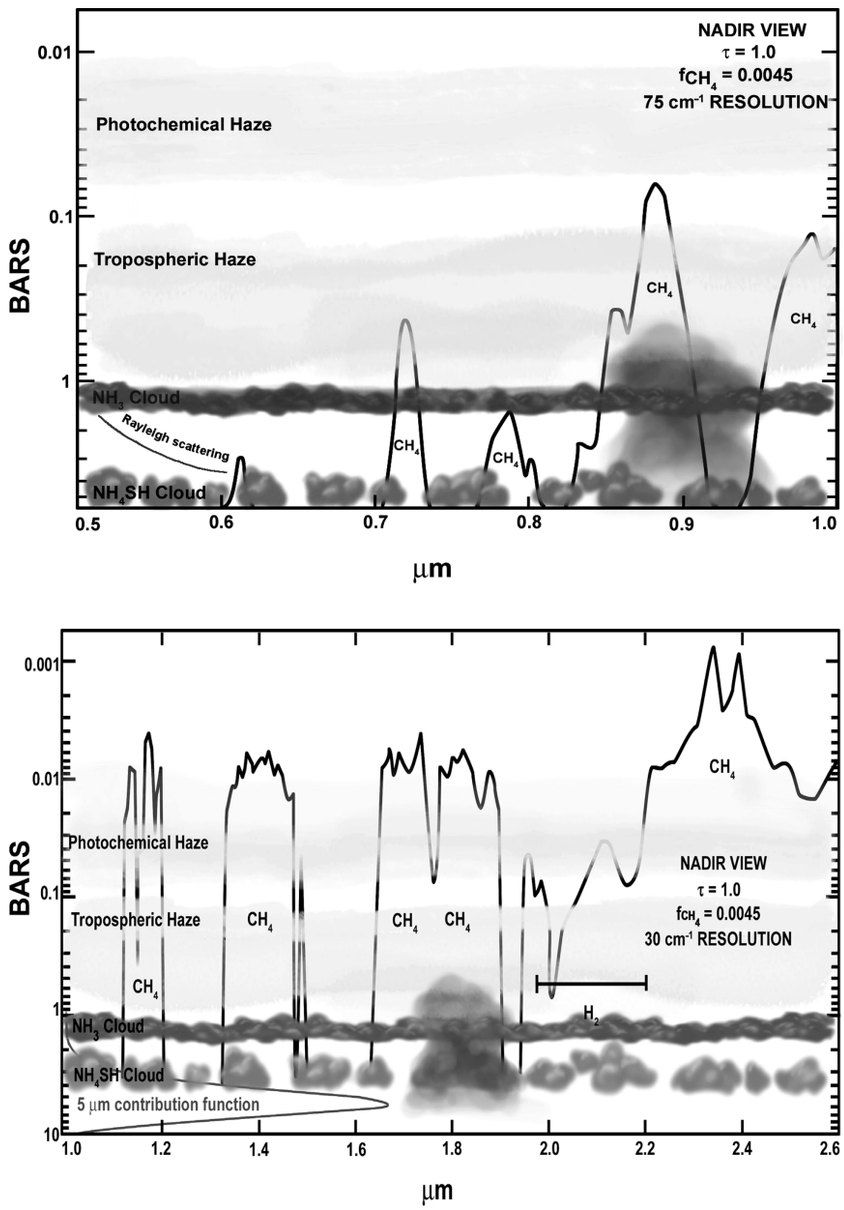


**Fig. 7.9** This figure gives an indication of the sounding level for Rayleigh scattering and for methane imaging and spectra assuming photons sound to optical depth $^1/_2$ (for a two-way path optical depth of 1), that the methane mole fraction is 0.0045, and for an instrumental resolution for the Cassini VIMS instrument. Expected levels of the condensate clouds are also indicated. The 5-μm thermal contribution function is also shown in the second panel defined by collision-induced hydrogen opacity (adapted from Baines et al. (2005))

model atmosphere. Many observations are obtained with CCD sensors and for these the model takes into account the Rayleigh scattering by the major gases in the atmosphere ($H_2$ and He) and the weak, moderate and strong absorption by $CH_4$ bands at 619, 727 and 890 nm, whose absorption coefficients are known (Karkoschka 1994, 1998). Layers of particles concentrated or mixed with the atmospheric gas are incorporated by specifying their phase functions (Mie or synthetic double Henyey–Greenstein function) and optical depths. For spherical Mie particles, the size parameter, particle sizes distributions and refractive indexes are included as free parameters. The problem with this method is that we are confronted with a multi-parametric fit and usually one must assume that some of the model parameters are reasonably constrained from other observations (e.g. polarimetry and infrared radiometry).

### 7.5.2 Mean Vertical Structure

In Table 7.2 we summarize the results on the vertical aerosol structure of Saturn from studies performed since 1970. The most recent analysis comes from the following sources: (1) Karkoschka and Tomasko (1992) who studied in detail low and high-resolution ground-based spectra (460–940 nm) obtained from 1986 to 1989. Karkoschka

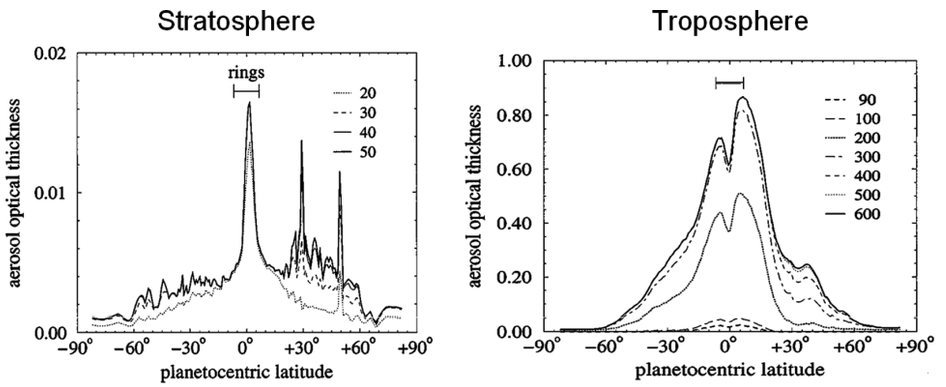


**Fig. 7.10** Optical depth profiles near equinox in 1995 (soon after northern summer) are shown for a variety of pressure levels from 20 to 600 mbar (from Stam et al. (2001))

**Table 7.2** Saturn's upper cloud and haze studies

| References | Observations | Epoch | Number of layers | Latitude range | Spectral coverage (μm) |
|---|---|---|---|---|---|
| Macy (1977) | Ground-based | ∼1970 | 3 | EZ–STZ | 0.3–1.1 |
| West (1983) | Ground-based | 1979 | 1 | 34°S–34°N | 0.619–0.937 |
| Tomasko and Doose (1984) | Pioneer 11 | 1979 | 2 | 25°S–55°N | 0.44/0.64 |
| West et al. (1983) | Voyager 2 | 1981 | 1–2 | NH | 0.264/0.75 |
| Karkoschka and Tomasko (1992) | Ground-based | 1986–1989 | 2 | NH | 0.46–0.94 |
| Karkoschka and Tomasko (1993) | HST | 1991 | 2 | NH | 0.3–0.89 |
| Ortiz et al. (1996) | Ground-based | 1991–1993 | 3 | NH | 0.6–0.96 |
| Kerola et al. (1997) | KAO | 1978 | 1–2 | Full Disk | 1.7–3.3 |
| Acarreta and Sánchez-Lavega (1999) | Ground-based | 1990 | 2 | EZ-NEB | 0.336–0.89 |
| Stam et al. (2001) | Ground-based | 1995 | 3 | NH/SH | 1.45–2.5 |
| Muñoz et al. (2004) | HST | 1997 | 3 | NH/SH | 0.23–0.89 |
| Temma et al. (2005) | Ground-based | 2002 | 2 | 10°S | 0.5–0.95 |
| Pérez-Hoyos et al. (2005, 2006a) | HST | 1994–2003 | 3 | SH | 0.255–1.042 |
| Karkoschka and Tomasko (2005) | HST | 1991–2004 | 3 | NH/SH | 0.23–2.37 |

NOTE: EZ = Equatorial Zone, STZ = South Temperate Zone, NEB = North Equatorial Belt, NH = Northern Hemisphere, SH = Southern Hemisphere

and Tomasko (1993) analyzed the structure of the stratospheric and tropospheric hazes using images obtained in the 300–889 nm wavelength range with the Hubble Space Telescope on July 1991. (2) Ortiz et al. (1996) studied the evolution of Saturn's hazes and clouds during the 1991–1993 period using ground-based images in the red methane bands and in their adjacent continuums (619–948 nm). (3) Kerola et al. (1997) presented a model of the clouds and hazes based on the near-infrared spectrum (1.7–3.3 μm wavelength range) obtained in 1978 with the Kuiper Airborne Observatory. (4) Temma et al. (2005) analyzed center-to-limb variations at many wavelengths for the Equatorial Zone. (5) Pérez-Hoyos et al. (2005) presented a study of the vertical structure of clouds and hazes in the upper atmosphere of Saturn's southern hemisphere during the 1994–2003 period, about one third of a Saturn's year, based on Hubble Space Telescope images in the spectral range between the near-UV (218–255 nm) and the near-IR (953–1042 nm), including the 890-nm methane band.

These studies envision an upper stratospheric haze and a tropospheric haze variable both with latitude and time (see Fig. 7.11). The tropospheric haze extends from the level $P_2$ close to the tropopause (∼90–100 mbar) to a level $P_1$ above the ammonia cloud (∼1.5–1.8 bar) and has an optical thickness $\tau_1$. Usually the haze phase function is modeled using a double Henyey–Greenstein function (Henyey and Greenstein 1941),

$$P(\theta) = f \cdot p(g_1, \theta) + (1 - f) \cdot p(g_2, \theta) \tag{7.2}$$

where

$$p(g, \theta) = \frac{1 - g^2}{(1 + g^2 - 2g\cos(\theta))^{3/2}} \tag{7.3}$$

Values to fit for the parameters that define this phase function are the single scattering albedo $\varpi_0$, and the three parameters $f$, $g_1$ and $g_2$ that determine the contributions to the forward and backward scattering are usually taken from

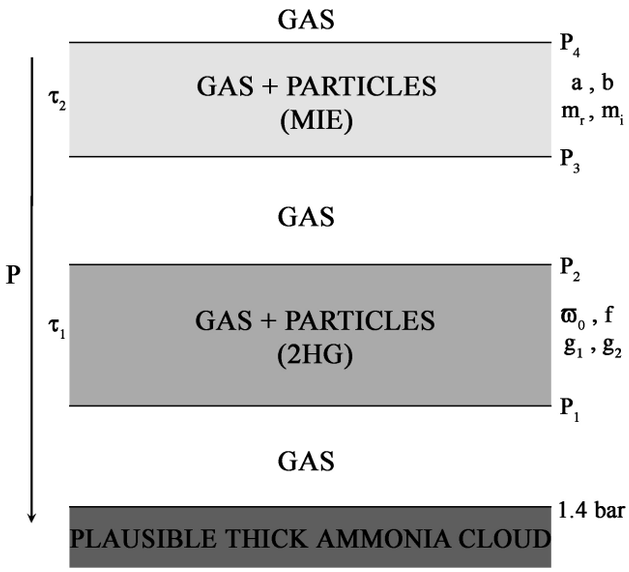


**Fig. 7.11** This schematic shows haze and cloud layers and lists parameters used in radiative transfer models employed in the analysis of ground-based and spacecraft images and spectra. For a definition of the parameters see the text (from Pérez-Hoyos et al. (2005))

Tomasko and Doose (1984) as shown in Table 7.1. Alternatively a Mie phase function is also used being characterized by the real and imaginary refractive indices $m_r$ and $m_i$, and the particle size distribution (with mean size $a$ and dispersion $b$, from Hansen 1971).

The stratospheric haze is located between pressure levels $P_3$ (∼10–90 mbar) and $P_4$ (∼1 mbar) and has an optical thickness $\tau_2$ that varies strongly with wavelength. All studies indicate that it is formed by small particles and a Mie phase function has been used to describe its behavior. The size distribution function used by Hansen and Travis (1974)

$$n(r) = r^{(1/b-3)} e^{-r/ab} \tag{7.4}$$

is found to be appropriate. Here $r$ is the particle's radius, $a \sim 0.15$–$0.2\,\mu$m is the effective (average) radius and $b = 0.1$ represents the variance in the size distribution. The small particle size implies that the optical depth $\tau_2$ is dependent of wavelength. The strong UV absorption indicates that at 300 nm $\varpi_o = 0.6 \pm 0.1$ (Karkoschka and Tomasko 1993; Pérez-Hoyos et al. 2005).

### 7.5.3 Latitudinal Structure

The banded visual appearance of Saturn and the alternating pattern of jet streams with latitude, suggest a regional classification of the haze content in three main latitude bands: the equator (between latitudes ±20°), the middle-latitudes (from 20° to 60°) and the polar region (from 60–70° to the pole). The stratospheric particles are smaller ($a \sim 0.1\,\mu$m) and more absorbent at UV wavelengths poleward of ∼70°, than at other latitudes. At other latitudes, particles are pretty similar with a mean particle radii near 0.2 μm.

The most important latitudinal variations take place in the tropospheric haze. There is a clear tendency to find darker particles at higher latitudes. This effect is most noticeable at 439 nm, a sensitive wavelength to single scattering. The pressure top level and especially the optical depth variations with latitude of this haze are the most important factor in generating the visual appearance of the planet. In the Equatorial Zone the haze is thicker and higher than elsewhere on the planet. At other latitudes the haze abundance is sharply reduced. In the polar region, the tropospheric haze diminished to only one tenth of its equatorial abundance (Pérez-Hoyos et al. 2005). These variations in haze altitude and thickness can be seen qualitatively in the strong 890-nm methane image (Fig. 7.12).

Karkoschka and Tomasko (2005) performed a principal-components study of 134 HST images obtained over the period 1991–2004. Their analysis included 18,000 center-to-limb curves in 30 filters from the near-UV to the near-IR. A small sample of the images is shown in Fig. 7.13. From these data four statistically-meaningful principal components emerged. The first principal variation is a strong mid-latitude variation of the aerosol optical depth in the upper troposphere. This structure shifts with Saturn's seasons, but the structure on small scales of latitude stays constant. This is what is most apparent in a casual comparison of images taken in different seasons. The second principal variation is a variable optical depth of stratospheric aerosols. The optical depth is large at the poles and small at mid- and low latitudes with a steep gradient between. This structure remains essentially constant in time. The third principal variation is a variation in the tropospheric aerosol size, which has only shallow gradients with latitude, but large seasonal variations. Aerosols are largest in the summer and smallest in the winter. The fourth principal variation is a feature of the tropospheric aerosols with irregular latitudinal structure and fast variability, on the time scale of months. This component is perhaps the most intriguing.

### 7.5.4 Short-term Changes

Smith et al. (1982) reported changes observed in the belt/zone pattern of Saturn between the two Voyagers encounters. Rapid changes affecting the brightness or color over an entire latitude band were observed in HST images between 1996 and 2003 (Pérez-Hoyos et al. 2006). These changes, in general, seem

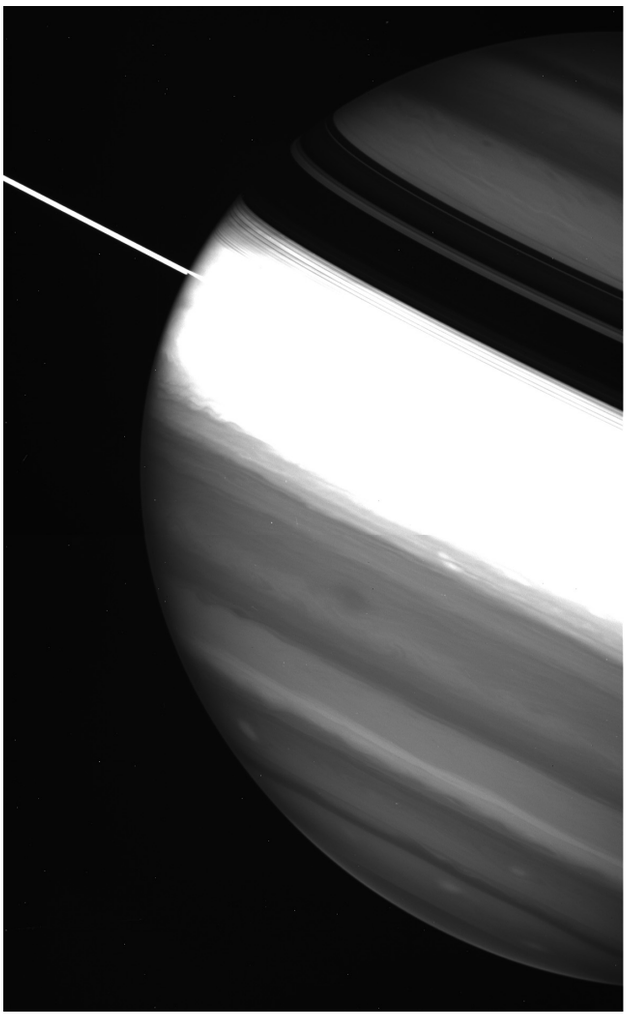

**Fig. 7.12** This Cassini ISS image taken with filter MT3 centered on the strong 890-nm methane absorption band shows qualitatively how cloud top altitude and optical thickness vary with latitude. The Equatorial Zone is a region of maximum vertical extent of the upper tropospheric haze and is artificially saturated in this image in order to make visible features in the darker mid- and high-latitude regions. Ring shadows in the northern hemisphere low latitudes should not be interpreted as methane absorption

not to be preceded by any individual atmospheric localized (in latitude or longitude) disturbance, evolving instead gradually and simultaneously in the whole band. Their origin is unclear, but the spectral behavior of the changes places the variability at the tropospheric haze level. They most frequently occur at equatorial and polar latitudes, and consist in the brightening or darkening by 5% to 10% of a latitude band with a width of 3° or less. About 80% of the observed phenomena produce a reflectivity variation less than 20% of the initial value. The vertical cloud structure modelling suggests variation of the single scattering albedo of the particles (probably induced by small changes in the size or composition of the particles) as the most likely explanation for most of the observed variations.

### 7.5.5 Seasonal Changes

Figure 7.14 shows that Saturn has gone through a full seasonal cycle starting with the 1979 measurements by the Pioneer IPP instrument (Tomasko and Doose 1984) and quantitative CCD imaging from the ground (West 1983). From those measurements and also from the Voyager color images and near-UV reflectivity obtained in 1981 (after equinox) it is clear that clouds and haze are higher and thicker in the northern mid-latitudes relative to the southern hemisphere near the end of southern summer and shortly after equinox (see Fig. 7.16 of Tomasko et al. 1984). The opposite asymmetry has prevailed thus far into the Cassini mission. During the early part of the Cassini tour beginning in 2004 Saturn's northern latitudes appeared blue, whereas the southern latitudes were yellow–red–brown. Methane absorption was stronger in the north. Both of these point to thinner, deeper haze and clouds in the north relative to the south. If the haze cycle is going to repeat in step with the seasonal phase a rapid shift in hemispheric asymmetry needs to occur very soon. Recent color changes are seen in Cassini images which indicate asymmetry reversal is underway in 2007–2008. A detailed cloud/haze microphysical model for the seasonal changes has not yet been developed but it seems likely that photochemical processes might play a role with seasonal modulation enhanced by ring shadowing. Other important processes might include seasonal changes in meridional circulation, sublimation of dirty ice grains exposed to sunlight and the atmospheric energy budget below the cloud tops.

### 7.5.6 Regional Structure: The Equatorial Jet

Figure 7.15 is a schematic diagram of the long-term structural changes in the tropospheric haze (from 70 mbar to 1.5 bar) of Saturn's Equatorial Zone (from 10°N to 10°S) as obtained from many studies over the period 1979–2004 (Pérez-Hoyos et al. 2005). A major change occurred following the giant storm in 1990 (GWS). In 1980–1981 the haze top was at a pressure $P_2 \sim 200$ mbar with optical thickness $\tau_1 \sim 10$ but in 2004 $P_2 \sim 40$ mbar and $\tau_1 \sim 15$. In general the haze is dense in the Equator (3.5°N and 0°) where it can reach an optical thickness of ∼30 decreasing to ∼7 at latitude 20°S. Observations at different wavelengths allow the detection of individual cloud tracers at different altitudes within this haze in the Equator (3° ± 2°N). For example Pérez-Hoyos and Sánchez-Lavega (2006a) placed

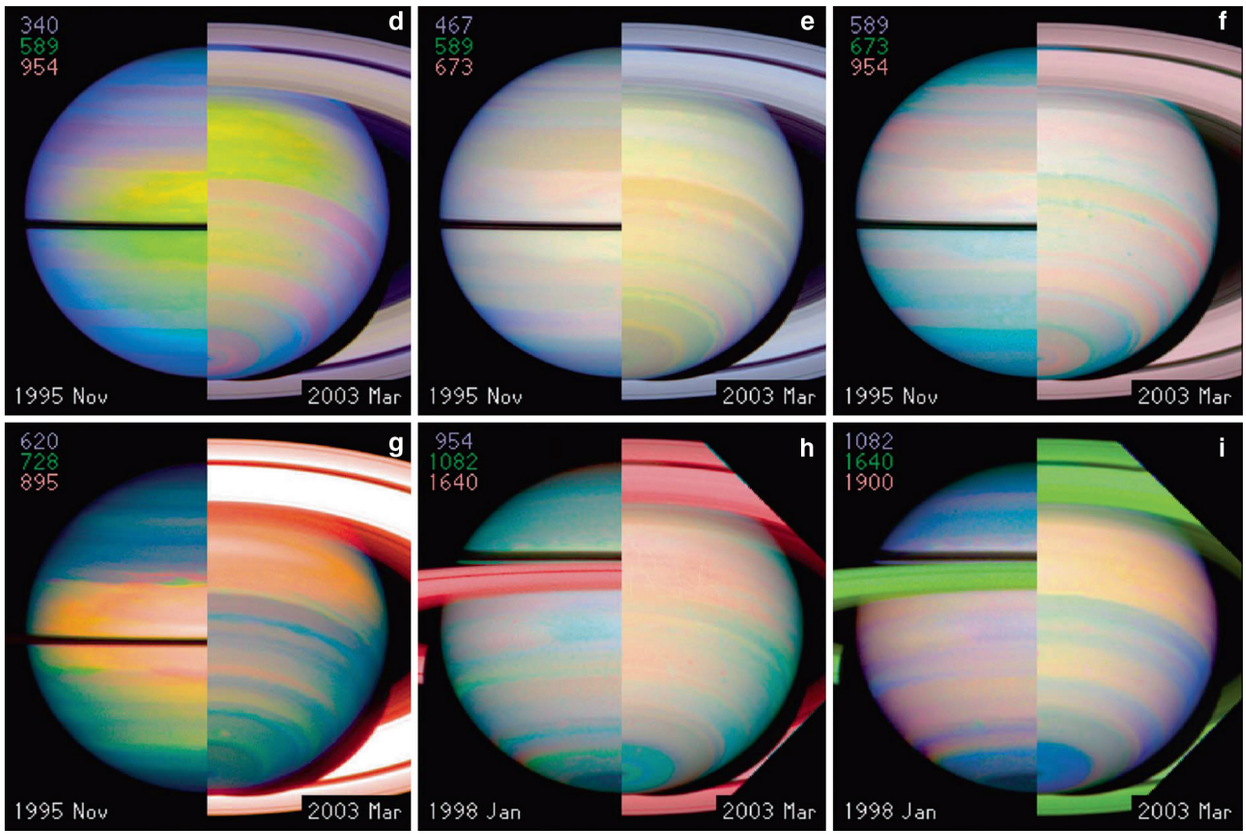


**Fig. 7.13** This figure shows a small sample of Hubble Space Telescope images used in the principal-components analysis of Karkoschka and Tomasko (2005). Images at a wide variety of wavelengths were inserted into the red, green, and blue color planes as indicated by the filter effective wavelength (nm) in the notation for each color composite, and images near equinox and near solstice were split and merged to show seasonal differences

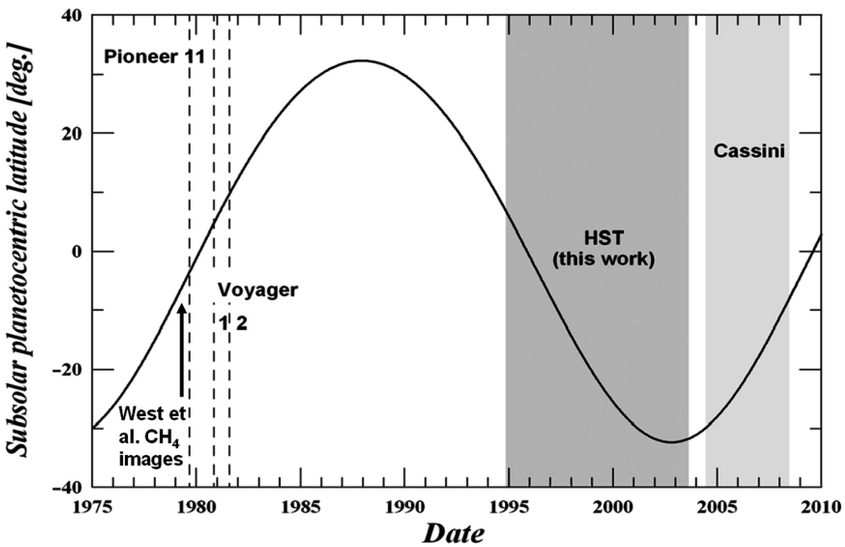


**Fig. 7.14** This figure shows the coverage of modern observations of Saturn over one seasonal cycle. The Cassini observations continue to the present and planning is underway to extend the mission to northern summer solstice in 2017 (adapted from Pérez-Hoyos et al. (2005))

them at a pressure level of 360 ± 140 mbar in 1980–1981 where the tracers moved with zonal velocities of 455 to 465 m/s. The 2004 analysis of HST images indicates that tracers were placed high in the atmosphere at 50 ± 10 mbar moving with zonal wind speeds of 280 ± 10 m/s (Pérez-Hoyos and Sánchez-Lavega 2006a). These results were confirmed by the first reflectivity measurements and models of the equatorial zone (from 8°N to 20°S) performed in 2004 and early

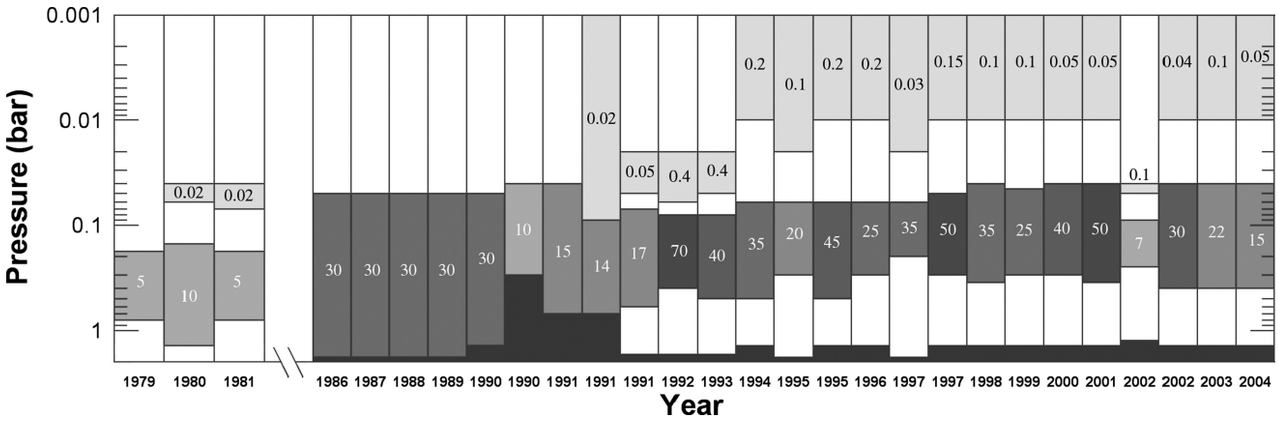


**Fig. 7.15** Derived optical depths and altitudes of upper tropospheric haze and clouds are shown as a function of observation epoch from 1979 to 2004 for a variety of cloud studies (from Pérez-Hoyos and Sánchez-Lavega (2006a))

2005 with Cassini-ISS instrument in the wavelength range from 250 to 950 nm (Sánchez-Lavega et al. 2007). Individual cloud elements were detected at two levels within the tropospheric haze, at 50 mbar moving with a speed of 263 $ms^{-1}$ and at 700 mbar moving at 364 $ms^{-1}$ (altitudes separated by 142 km), representing a vertical shear of the zonal wind of 40 $ms^{-1}$ per scale height. A comparison with the previous analysis indicates that the equatorial jet has undergone a significant intensity change between 1980–1981 and 1996–2005, most probably as a consequence of the large-scale equatorial storms that occurred in 1990 and 1994–1996.

### 7.5.7 Regional Structure: The Great White Spot (GWS)

In September 1990 (Fig. 7.16) a giant storm (the "Great White Spot", GWS) erupted in Saturn's Equatorial Zone at 5°N latitude, disturbing the dynamics and cloud structure of this region during more than a year (Sánchez-Lavega et al. 1991, 1993, 1994; Beebe et al. 1992; Barnet et al. 1992). Radiative transfer models indicated that cloud tops elevated by 1.2–1.5 scale heights during the onset and mature storm stage relative to the undisturbed atmosphere, descending later during the evolved phase by 0.7 scale heights relative to the altitude of the mature clouds. The single-scattering albedo of the particles in the UV-blue wavelengths increased significantly during the onset and mature stages of the storm (Westphal et al. 1992; Barnet et al. 1992). In 1994 another large cloud system erupted but not as large as one in 1990. The cumulative effects of these events produced elevated optical depths in the equatorial zone for years afterward.

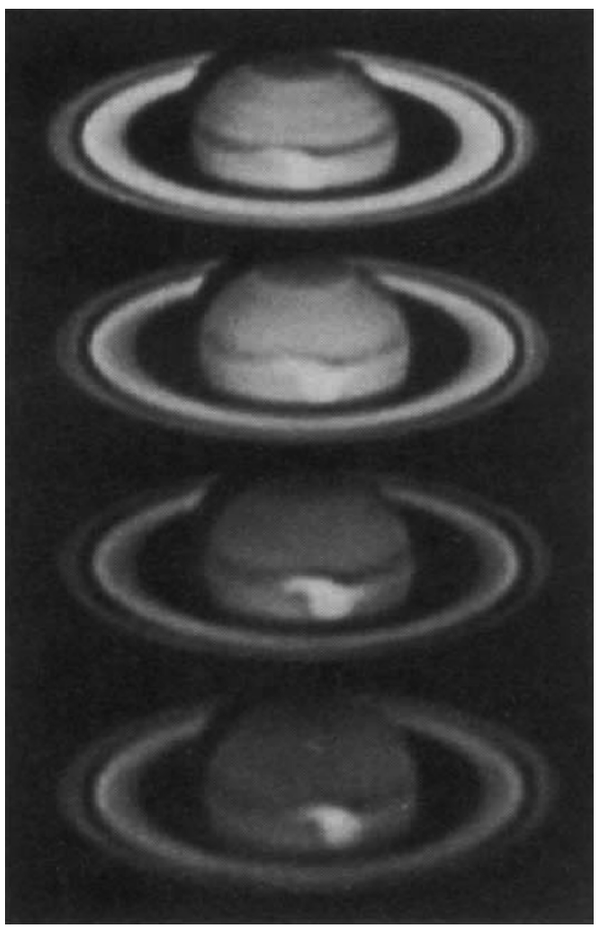

**Fig. 7.16** These panels show some of the ground-based images of the Great White Spot eruption of 1990. From top to bottom in red, green, blue and ultraviolet wavelengths (Pic-du-Midi Observatory, France). Blue-filter and UV images show the highest contrast between the bright spot and the dark ambient haze structure (from Sánchez-Lavega et al. (1991))

### 7.5.8 Regional Structure: The South Polar Vortex

A warm cap in the South Pole of Saturn (Orton and Yanamandra-Fisher 2005) is the site of a large vortex that surrounds the pole at latitude 87°S (Sánchez-Lavega et al. 2006). High-resolution images of the cap obtained with Cassini ISS and VIMS instruments (Fig. 7.17) show that it is a hole in the cloud layer with altitude differences in the eye wall of 40 km (inner wall) and 70 km (outer wall) as measured from the projected shadows (Dyudina et al. 2008). Radiative transfer models for latitudes poleward of 80°S show that the polar stratospheric haze is formed by ultraviolet–violet absorbing particles with a mean radius of 0.15 μm extending between the pressure levels ∼1 and 30 mbar (Sánchez-Lavega et al. 2006a). A lower tropospheric haze layer formed by particles with a radius of ∼1 μm resides between 70 and 150–300 mbar but it is thin compared to other areas of Saturn with optical thickness of ∼1 being neutral in its wavelength dependence.

### 7.5.9 Convective Clouds

The 5-μm panel in Fig. 7.17 probes the deepest levels (see the contribution function in Fig. 7.9) and cloud opacity is revealed by its ability to block upwelling thermal radiation. Sounding depth at other wavelengths sensitive to reflected sunlight can also be judged from Fig. 7.9. Many small-scale features can be seen in the 0.75-μm continuum image indicating that photons are penetrating deeply at that wavelength. Some of the same features can be seen even in the 0.46-μm image. Note that some small-scale features are brighter than the atmosphere they are embedded in (consistent with the idea that they are relatively dense clouds composed of white ammonia ice) but some are darker than their surroundings. The oval near the lower-left corner of each panel is bright in the blue image but dark in the near-infrared images. This is opposite the color behavior of most chromophore material. The absence of these features in the methane absorption bands shows that they reside in the deeper atmosphere, probably deeper than the 2-bar pressure level. The morphology of these features resembles terrestrial cumulus and is suggestive of formation in a freely convecting atmosphere, hence we call these convective clouds.

The Cassini VIMS ability to probe to deep levels at all latitudes and in polar night has opened up a new realm for investigation of deeper cloud features. Information on winds revealed by these images is discussed in Chapter 6. These studies are in their early phases and we give here some samples of what can be seen. Global views of Saturn in the 5-μm band are seen in Fig. 7.18. Hundreds of small cloud features can be seen. The overlying clouds are slightly thicker in the southern hemisphere in the 2005 image (panel b) as noted earlier in the section on seasonal asymmetry. Few convective clouds can be seen in the Equatorial Zone where a more zonally-uniform cloud prevails. The northern-hemisphere view in the left panel shows a series of cloud-free 'holes' in the retrograde jet at 33.5° latitude (planetocentric). Each is about 800 km in diameter. Images in the wavelength range 3.1–5.1 μm are sensitive to the slope in the particle extinction cross section. Fig. 7.19 reveals distinct bands of increasing upper troposphere cloud opacity with the lowest opacity at the highest latitudes.

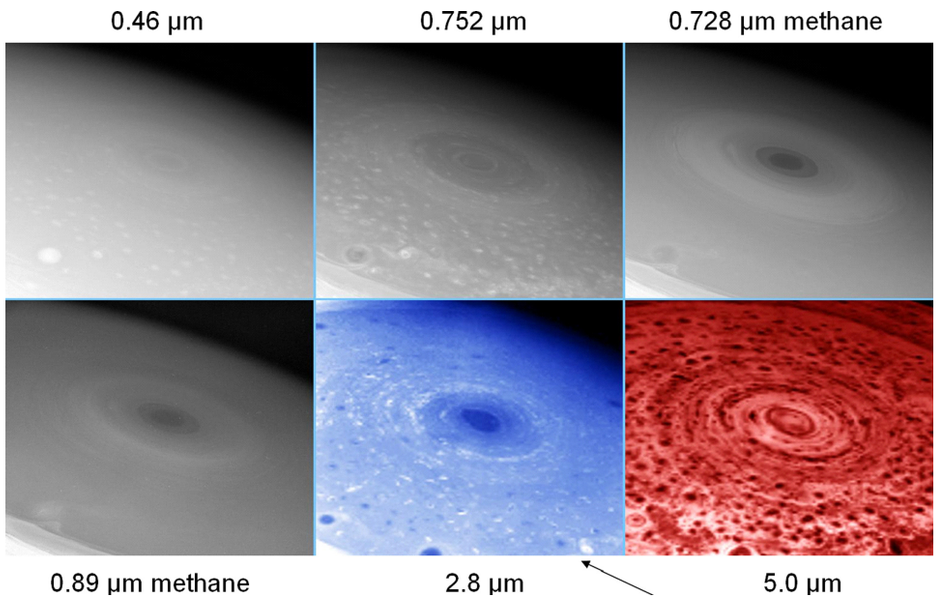


**Fig. 7.17** Six panels from the Cassini VIMS experiment show views of the southern polar vortex and surrounding region from visible wavelengths to 5 μm (from Baines et al. (2008))

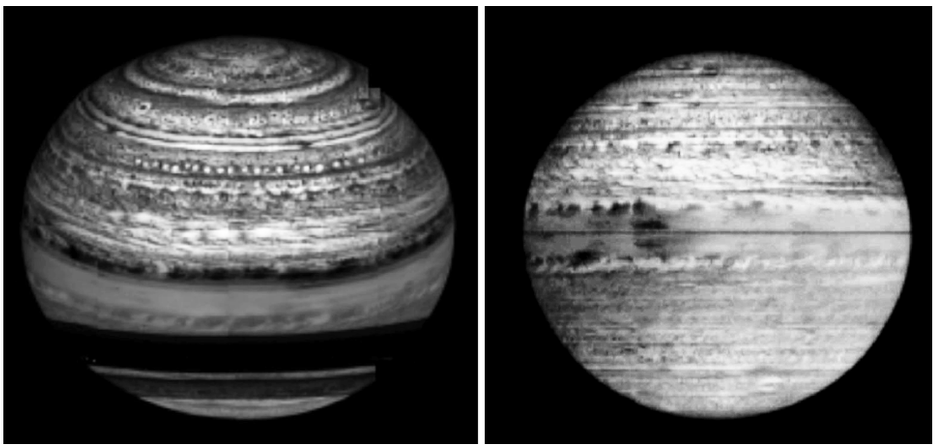

**Fig. 7.18** Global views of Saturn at 5 μm show many details of the convective clouds in the 2–4 bar region. In the left panel Saturn's "String of Pearls" observed over 2.8 years. Observed in Saturn's thermal glow at 5 μm, a train of nearly regularly spaced holes in the clouds are repeatedly observed throughout the Cassini mission thus far, for more than 2.8 years, near 33.5° latitude (planetocentric). The holes are spaced about 3500 km (4.4° in longitude) apart, span about 1° (800 km) each, and are confined to a latitude range of <2° of latitude, 110° longitude. The right panel shows Saturn's hemispheric asymmetry (on average the intensities are slightly lower and convective clouds slightly less visible due to overlying haze). This effect is masked by scattered sunlight which elevates the intensities mostly in the southern hemisphere. The ring shadow darkens part of the northern hemisphere, right side (from Baines et al. (2008))

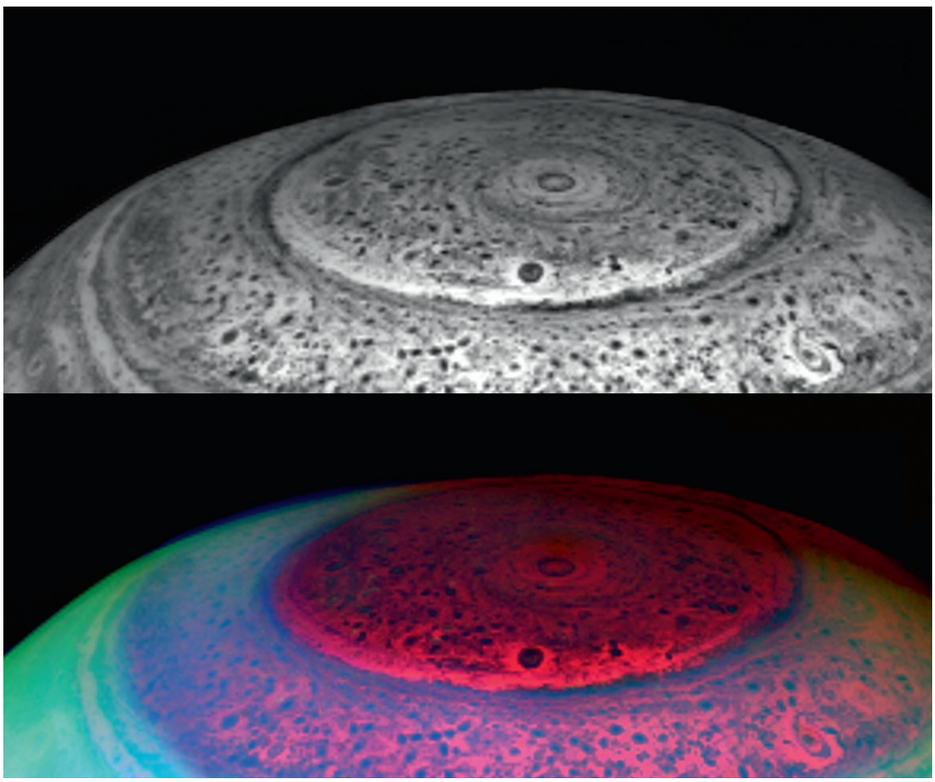

**Fig. 7.19** Near-infrared views of the south pole of Saturn. Detailed views are shown as acquired on May 11, 2007 by Cassini/VIMS, from a vantage point 0.36 million km above the cloud tops. Saturn's upwelling thermal radiation at 5.1 μm illuminates the atmosphere from below, revealing deep cloud features in silhouette (*top panel*). Thermal radiation at 5.1 μm populates the red color plane in the bottom panel. Overlying haze reflects sunlight, shown as blue (3.1 μm) and green (4.1 μm), especially equatorward of the cloudy band circling the planet near 75° south latitude (from Baines et al. (2008))

## 7.6 Solar Radiation Penetration and Deposition

Radiative heating/cooling is a fundamental process for the general circulation of Saturn and for other dynamical phenomena. Tomasko and Doose (1984) estimated geometric albedo (the ratio of flux reflected in the back-scatter direction to that for a flat surface of equal area and having the Lambert reflection law) and phase integral for the Equatorial Zone and a mid-latitude belt. For global radiation budget the spherical albedo is a key parameter. It is the ratio of power reflected in all directions to incident power for a spherical body. It is the product of the geometric albedo and the phase integral and these are reported in Table 7.1.

The insolation at the top of Saturn's atmosphere at a given time and latitude including the effect of Saturn's oblateness, ring shadowing and the solar radiation scattered from the rings to the atmosphere, was first addressed by Brinkman and McGregor (1979) and later by Barnet et al. (1992). Pérez-Hoyos and Sánchez-Lavega (2006b) recalculated the distribution map of daily averaged insolation along a Saturn's year for a solar constant of $S_0 = 15\,\mathrm{Wm}^{-2}$ to study the solar flux deposition in the optical wavelength range from 0.25 to 1.0 μm, a spectral band that covers about 70% of the solar radiation power. The solar flux deposition is controlled by gaseous absorption in the methane-bands and by Rayleigh scattering in the continuum (much less important are the absorptions due to ammonia bands and $H_2$ quadrupole lines), and more importantly by scattering and absorption by the aerosols. Radiative transfer calculations that include the internal radiation fields shows that the maximum heating level is ∼250 mbar for these wavelengths, substantially higher than previously expected because of the huge optical thickness of the tropospheric haze described in all vertical cloud structure models. Given that our spectral range accounts for about the 70% of the total solar flux, and using previous estimates for the penetration levels of infrared radiation in Saturn's atmosphere, Pérez-Hoyos and Sánchez-Lavega (2006b) concluded that almost no solar radiation will heat the levels deeper than 600 mbar. This conclusion may need to be revised in light of the recent Cassini data which show contrasts from convective clouds that are probably deeper than 600 mbar.

Once the solar flux daily mean is calculated as a function of altitude $F(P)$, the heating rate is obtained from

$$\frac{dT}{dt} = \frac{g}{C_p}\frac{dF}{dP} \tag{7.5}$$

being $g$ the local acceleration of gravity and $C_p\,(P)$ the specific heat at constant pressure. Typical values of tropospheric heating for equatorial latitudes are 0.2 K/day, whereas for mid-latitudes they decrease to 0.04–0.08 K/day. Polar tropospheric heating rates are small, not greater than 0.02 K/day.

## 7.7 Summary and Future Work

Observations and analyses of ground-based and spacecraft data obtained during the past three decades has led to a picture of Saturn's cloud and haze with many components covering a wide range in spatial and temporal scales. The deepest clouds trace small-scale convective activity and are seen at some latitudes all the way into the blue but are most easily seen in thermal emission at 5 μm. Examination of Figs. 7.17 through 7.19 reveals morphological forms which vary with latitude. These morphological differences may provide good clues regarding instability modes, wind shear and other attributes of dynamics on the scale of zonal jets and smaller. This information has not yet been exploited.

Observations at many wavelengths and over a significant part of Saturn's seasonal cycle reveal seasonal and nonseasonal variations. Some variations have short time scales. Recent Cassini images show that Saturn's hemispheric asymmetry is changing, in expectation with observations taken in 1979 which show an asymmetry opposite to what was observed by Cassini instruments until 2008. Over the next year the asymmetry reversal is expected to be complete with the hope that frequent and detailed Cassini observations will allow us to construct a more detailed picture of how the process unfolds.

On regional scales three latitude bands are distinct. The Equatorial Zone is consistently a region of higher and thicker clouds. It is also a region which experiences occasional major cloud eruptions which have long-term influences on cloud opacity. Images at 5 μm do not show this region to be populated with convective clouds. Rather, the haze is more uniform, possibly because of strong zonal wind shear. Middle latitudes experience strong seasonal variations. High latitudes are regions where the upper tropospheric opacity is low, convective clouds and small vortices are numerous, and where a polar vortex produces an extreme low in aerosol opacity right at the pole.

In the vertical domain the atmosphere exhibits two distinct regions – upper troposphere and stratosphere. Upper tropospheric cloud particles are larger than the wavelength, although how much larger is still not settled. Above that lies an optically thin layer of particles which are significantly smaller than visible wavelengths. Within the polar vortex region these particles are dark at UV wavelengths, more abundant than at lower latitudes, and exhibit strong positive polarization similar to jovian polar aerosols which West and Smith (1991) proposed to be aggregates of small monomers.

Their origin is probably tied to auroral energy deposition and their composition may be different than that of the main stratospheric haze at lower latitudes. A first positive identification of hydrocarbon composition was made with a stellar occultation measurement (Nicholson et al. 2006). Diphosphine haze should be abundant in the lower stratosphere based on photochemical considerations and the observation that the phosphine mixing ratio decreases with altitude.

In spite of these advances some questions remain essentially unanswered, or at least the proposed solutions are still very much open to debate. One of the major puzzles continues to be the lack of spectral evidence for ammonia ice. Atreya et al. (2005) and Kalogerakis et al. (2008) propose coating of ammonia ice particles by photochemical products (for Jupiter, with extension to Saturn). This is the inverse of the traditional picture that photochemical aerosol sedimenting from high altitude might serve as condensation nuclei for ammonia ice particles (West et al. 1986, for Jupiter, with extension to Saturn). If this mechanism can account for the masking of ammonia ice signatures the production rate of the photochemical product must outstrip the production rate of ammonia ice. It is not obvious that this can be the case. A detailed microphysical model which includes ammonia condensation might help assess this proposal. It might also help us understand why some small-scale cloud features are dark (i.e. abundant in chromophore material).

Instruments on Cassini continue to acquire data and much of the existing Cassini data has yet to be comprehended. In the coming years we can expect to gain a much better understanding of the details of seasonal change. Observations at many phase angles and many latitudes (most notably low latitudes which are obscured by the rings or ring shadow except for short times) will allow us to improve on models of the radiation budget which require observations at many phase angles. We are still using values of the phase function and phase integral based on the 1979 Pioneer data. Images of Saturn's limb at high spatial resolution will provide detailed vertical profiles of the stratospheric haze. Additional stellar and solar occultations will yield detailed profiles and compositional information on the stratospheric haze. Ultimately we can expect these new data and analyses to illuminate the important chemical and physical processes which take place over many scales in space and time.

## References


Acarreta, J.R., Sánchez-Lavega, A. Vertical cloud structure in Saturn's 1990 Equatorial Storm, Icarus 137, 24–33 (1999).

Atreya, S.K., Wong, A.-S. Coupled clouds and chemistry of the giant planets – a case for multiprobes. Space Sci. Rev. 116, 121–136 (2005).

Atreya, S.K., Wong, A.-S., Baines, K.H., Wong, M.H., Owen, T.C. Jupiter's ammonia clouds – localized or ubiquitous? Planet. Space Sci. 53, 498–507 (2005).

Baines, K.H., Carlson, R.W., Kamp, L.W. Fresh ammonia ice clouds in Jupiter: I. Spectroscopic identification, spatial distribution, and dynamical implications. Icarus 159, 74–94 (2002).

Baines, K.H., Drossart, P., Momary, T.W., Formisano, V., Griffith, C., Bellucci, G., Bibring, J.-P., Brown, R.H., Buratti, B.J., Capaccioni, F., Cerroni, P., Clark, R.N., Coradini, A., Cruikshank, D.P., Jaumann, R., Langevin, Y., Matson, D.L., McCord, T.B., Mennella, V., Nelson, R.M., Nicholson, P.D., Sicardy, B., Sotin, C. The atmospheres of Saturn and Titan in the near-infrared: First results of Cassini/VIMS. Earth Moon Planets 96, 119–147 (2005).

Baines, K.H., Momary, T.W., Kim J.H., Ross-Serote, M., Showman, A.P., Atreya, S.K., Brown, R.H., Buratti, B.J., Clark, R.N., Nicholson, P.D. Saturn's dynamic atmosphere at depth: Physical characteristics, winds, and spatial constraints on trace gas variability near the 3-bar level and their dynamical implications from Cassini-Huygens/VIMS. Poster Presented at Saturn after Cassini-Huygens, Conference, Imperial College, London, United Kingdom, July 28–August 1 (2008).

Baines, K.H., Delitsky, M.L., Momary, T.W., Brown, R.H., Buratti, B.J., Clark, R.N., Nicholson, P.D. Storm clouds on Saturn: Lightning-induced chemistry and associated materials consistent with Cassini/VIMS spectra. Planetary and Space Sci. in press (2009).

Banfield, D., Conrath, B.J., Gierasch, P.J., Nicholson, P.D., Mathiews, K. Near-IR spectrophotometry of jovian aerosols: Meridional and vertical distributions. Icarus 134, 11–23 (1998).

Barnet, C.D., Westphal, J.A., Beebe, R.F., Huber, L.F. Hubble Space Telescope observations of the 1990 equatorial disturbance on Saturn: Zonal winds and central meridian albedos. Icarus 100, 499–511 (1992).

Beebe, R.F., Barnet, C., Sada, P.V., Murrell, A.S. The onset and growth of the 1990 equatorial disturbance on Saturn. Icarus 95, 163–172 (1992).

Brinkman, A.W., McGregor, J. The effect of the ring system on the solar radiation reaching the top of Saturn's atmosphere: Direct radiation. Icarus 38, 479–482 (1979).

Brooke, T.Y., Knacke, R.F., Encrenaz, T., Drossart, P., Crisp, D., Feuchtgruber, H. Models of the ISO 3-μm reflection spectrum of Jupiter. Icarus 136, 1–13 (1998).

Dyudina, U.A. Ingersoll, A.P., Ewald, S.P., Vasavada, A.R., West, R.A., Del Genio, A.D., Barbara, J.M., Porco, C.C., Achterberg, R.K., Flasar, F.M., Simon-Miller, A.A., Fletcher, L.N. Dynamics of Saturn's south polar vortex. Science 319, 1801 (2008).

Friedson, A.J., Wong, A.S., Yung, Y.L., Models for polar haze formation in Jupiter's stratosphere. Icarus 158, 389–400 (2002).

Hansen, J.E. Multiple scattering of polarized light in planetary atmospheres. Part I. The doubling method. J. Atmos. Sci. 28, 120–125 (1971).

Hansen, J.E., Travis, L.D. Light scattering in planetary atmospheres. Space Sci. Rev. 16, 527–610 (1974).

Henyey, L.G., Greenstein, J.L. Diffuse radiation in the galaxy. Annales d'Astrophysique 3, 117–137 (1941).

Huffman, D.R., Bohren, C.F. Infrared absorption spectra of nonspherical particles treated in the Rayleigh-ellipsoid approximation. In: D. Schuerman (ed) Light Scattering by Irregularly Shaped Particles, Plenum, New York, pp. 103–111 (1980).

Kalogerakis, K.S., Marschall, J., Oza, A.U., Engel, P.A., Meharchand, R.T., Wong, M.H., The coating hypothesis for ammonia ice particles in Jupiter: Laboratory experiments and optical modeling. Icarus 196, 202–215 (2008).

Karkoschka, E. Spectrophotometry of the jovian planets and Titan at 300- to 1000-nm wavelength: The methane spectrum. Icarus 111, 174–192 (1994).

Karkoschka, E. Methane, ammonia, and temperature measurements of the jovian planets and Titan from CCD-spectrophotometry. Icarus 133, 134–146 (1998).

Karkoschka, E., Tomasko, M.G. Saturn's upper troposphere 1986–1989. Icarus 97, 161–181 (1992).

Karkoschka, E., Tomasko, M.G. Saturn's upper atmospheric hazes observed by the Hubble Space Telescope. Icarus 106, 421–441 (1993).

Karkoschka, E., Tomasko, M. Saturn's vertical and latitudinal cloud structure 1991–2004 from HST imaging in 30 filters. Icarus 179, 195–221 (2005).

Kerola, D.X., Larson, H.P., Tomasko, M.G. Analysis of the near-IR spectrum of Saturn: A comprehensive radiative transfer model of its middle and upper troposphere. Icarus 127, 190–212 (1997).

Lewis, J.S. The clouds of Jupiter and the $NH_3 - H_2O$ and $NH_3 - H_2S$ systems. Icarus. 10, 365–378 (1969).

Macy, W. Inhomogeneous models of the atmosphere of Saturn, Icarus 32, 328–347 (1977).

Martonchik, J.V., Orton, G.S., Appleby, J.F. Optical properties of $NH_3$ice from the far infrared to the near ultraviolet. Appl. Opt. 23, 541–547 (1984).

Muñoz, O., Moreno, F., Molina, A., Grodent, D., Gerard, J.C., Dols, V. Study of the vertical structure of Saturn's atmosphere using HST/WFPC2 images. Icarus 169, 413–428 (2004).

Nicholson, P., Hedman, M.M., Gierasch, P.J., the Cassini VIMS Team, Probing Saturn's Atmosphere with Procyon, Bull. Amer. Astron. Soc. 38, 555 (2006).

Ortiz, J.L., Moreno, F., Molina, A. Saturn 1991–1993: Clouds and hazes. Icarus 119, 53–66 (1996).

Orton, G.S., Yanamandra-Fisher, P. Saturn's temperature field from high-resolution middle-infrared imaging. Science 307, 696–698 (2005).

Pérez-Hoyos, S., Sánchez-Lavega, A., French, R.G., Rojas, J.F. Saturn's cloud structure and temporal evolution from ten years of Hubble Space Telescope images (1994–2003). Icarus 176, 155–174 (2005).

Pérez-Hoyos, S., Sánchez-Lavega, A. On the vertical wind shear of Saturn's equatorial jet at cloud level. Icarus 180, 161–175 (2006a).

Pérez-Hoyos, S., Sánchez-Lavega, A. Solar flux in Saturn's atmosphere: maximum penetration and heating rates in the aerosol and cloud layers", Icarus, 180, 368–378 (2006b).

Pérez-Hoyos, S., Sánchez-Lavega, A., French, R.G. Short-term changes in the belt/zone structure of Saturn's Southern Hemisphere (1996–2004). Astron. Astroph. 460, 641–645 (2006).

Pope, S.K., Tomasko, M.G., Williams, M.S., Perry, M.L., Doose, L.R., Smith, P.H. Clouds of ammonia ice: Laboratory measurements of the single-scattering properties. Icarus 100, 203–220 (1992).

Pryor, W.R., Hord, C.W. A study of photopolarimeter system UV absorption data on Jupiter, Saturn, Uranus, and Neptune: Implications for Auroral Haze formation. Icarus 91, 161–172 (1991).

Sánchez-Lavega, A. Saturn's great white spots, Chaos 4, 341–353 (1994).

Sánchez-Lavega, A., Colas, F., Lecacheux, J., Laques, P., Miyazaki, I., Parker, D. The Great white Spot and disturbances in Saturn's equatorial atmosphere during 1990. Nature 353, 397–401 (1991).

Sánchez-Lavega, A., Lecacheux, J., Colas, F., Laques, P. Temporal behavior of cloud morphologies and motions in Saturn's atmosphere, J. Geophys. Res. E10, 18857–18872 (1993).

Sánchez-Lavega, A., Lecacheux, J., Colas, F., Laques, P. Photometry of Saturn's 1990 equatorial disturbance, Icarus 108, 158–168 (1994).

Sánchez-Lavega, A., Hueso, R., Pérez-Hoyos, S., Rojas, J. F., A strong vortex in Saturn's South Pole, Icarus 184, 524–531 (2006).

Sánchez-Lavega, A., Hueso, R., Pérez-Hoyos, S. The three-dimensional structure of Saturn's equatorial jet at cloud level, Icarus 187, 510–519 (2007).

Smith, B.A., Soderblom, L., Batson, R., Bridges, P., Inge, J., Masursky, H., Shoemaker, E., Beebe, R., Boyce, J., Briggs, G., Bunker, A., Collins, S.A., Hansen, C.J., Johnson, T.V., Mitchell, J.L., Terrile, R.J., Cook, A.F., Cuzzi, J., Pollack, J.B., Danielson, G.E., Ingersoll, A.P., Davies, M.E., Hunt, G.E., Morrison, D., Owen, T., Sagan, C., Veverka, J., Strom, R., Suomi, V.E. A New Look at the Saturn system: The Voyager 2 images. Science 215, 504–537 (1982).

Stam, D.M., Banfield, D., Gierasch, P.J., Nicholson, P.D., Matthews, K., Near-IR Spectrophotometry of Saturnian Aerosols—Meridional and Vertical Distribution, Icarus 152, 407–422 (2001).

Temma, T., Chanover, N.J., Simon-Miller, A.A., Glenar, D.A., Hillman, J.J., Khuen, D.M. Vertical structure modeling of Saturn's equatorial region using high spectral resolution imaging, Icarus 175, 464–489 (2005).

Tomasko, M.G., Doose, L.R., Polarimetry and photometry of Saturn from Pioneer 11: observations and constraints on the distribution and properties of cloud and aerosol particles. Icarus 58, 1–34 (1984).

Tomasko, M.G., West, R.A., Orton, G.S., Tejfel, V.G. Clouds and aerosols in Saturn's atmosphere, in T. Gehrels, M.S. Matthews (eds) Saturn, University of Arizona Press, Tucson, pp. 150–194 (1984).

Weidenschilling, S.J., Lewis, J.S. Atmospheric and cloud structures on the jovian planets. Icarus 20, 465–476 (1973).

West, R.A. Spatially resolved methane band photometry of Saturn II. Cloud structure models at four latitudes. Icarus 53, 301–309 (1983).

West, R.A., Smith, P.H. Evidence for aggregate particles in the atmospheres of Titan and Jupiter, Icarus 90, 330–333 (1991).

West, R.A., Sato, M., Hart, H., Lane, L.A., Hord, C.W., Simmons, K.E., Esposito, L.W., Coffeen, D.L., Pomphrey, R.B. Photometry and polarimetry of Saturn at 2640 and 7500 Å. J. Geophys. Rev. 88, 8679–8697 (1983).

West, R.A., Strobel, D.F., Tomasko, M.G. Clouds, aerosols, and photochemistry in the jovian atmosphere. Icarus 65, 161–217 (1986).

West, R.A., Orton, G.S., Draine, B.T., Hubbell, E.A., Infrared absorption features for tetrahedral ammonia ice crystals. Icarus 80, 220–224 (1989).

West, R.A., Baines, K.H., Friedson, A.J., Banfield, D., Ragent, B., Taylor, F.W. Jovian clouds and haze. In: F. Bagenal, T.E. Dowling, W.B. McKinnon (eds) Jupiter: The Planet, Satellites and Magnetosphere, Cambridge University Press, Cambridge (2004).

Westphal, J.A., Baum, W.A., Ingersoll, A.P., Barnet, C.D., De Jong, E.M., Danielson, G.E. Hubble Space Telescope observations of the 1990 equatorial disturbance on Saturn: Images, albedos, and limb darkening, Icarus 100, 485–498 (1992).

Wong, A.-S., Yung, Y.L., Friedson, A.J. Benzene and haze formation in the polar atmosphere of Jupiter. Geophys. Res. Lett. 30 (2003).

Wong, M., Bjoraker, G., Smith, M. Flasar, D., Nixon, C. Identification of the 10-μm ammonia ice feature on Jupiter. Planet. Space Sci. 52, 385–395 (2004).